Semina Ciências Exatas e Tecnológicas

e-ISSN 1679-0375
ENGINEERING

ORIGINAL ARTICLE DOI 10.5433/1679-0375.2025.v47.53878

iThenticate

Numerical and Analytical Study of an Electric Motor Cooling System

Estudo Numérico e Analítico de um Sistema de Arrefecimento de um Motor Elétrico

Miguel Costa[1], Alexandre M. Afonso[2]

Received: September 23, 2025 *Received in revised form: December 13, 2025* *Accepted: January 27, 2026* *Available online: February 23, 2026*

ABSTRACT

The growing demand for efficiency, decarbonization, and sustainability has placed electric motors at the forefront of industrial innovation, driving the need for high performance with minimal size and enhanced energy efficiency. Since motors lose energy mainly as heat through Joule losses in the stator and rotor, effective cooling is essential to achieve higher power density without compromising performance. This study investigated heat transfer in IC511 motors with tube cooling systems using analytical and numerical approaches. The analytical study showed that higher airflow speeds consistently improve cooling, with fan type and rotational speed having the greatest impact, while tube length, diameter, and operating temperatures were less influential. Numerical simulations revealed that front deflectors reduced heat transfer by 21%, the use of Variable Speed Drive operation at low speeds decreased it by 15% to 71%, and smaller fans caused a 26% reduction, whereas end shield modifications improved cooling by approximately 6%, and removing up to 24 tubes maintained heat removal, suggesting cost-saving potential. Overall, the study advances understanding of thermal behavior in tube-cooled motors and identifies critical design parameters to optimize performance and sustainability.

keywords electric motor, heat transfer, air cooling, analytical, computational fluid dynamics

RESUMO

A crescente procura por eficiência, descarbonização e sustentabilidade colocou os motores elétricos na vanguarda da inovação industrial, impulsionando a necessidade de elevado desempenho com dimensões reduzidas e maior eficiência energética. Como os motores perdem energia principalmente sob a forma de calor devido a perdas de Joule no estator e rotor, a refrigeração eficaz é essencial para alcançar maior densidade de potência sem comprometer o desempenho. Este estudo investigou a transferência de calor em motores IC511 com sistemas de refrigeração por tubos, utilizando abordagem analítica e numérica combinada. O estudo analítico mostrou que velocidades de fluxo mais elevadas melhoram consistentemente a refrigeração, com o tipo de ventilador e a velocidade de rotação a terem o maior impacto, enquanto o comprimento do tubo, o diâmetro e as temperaturas de operação foram menos influentes. As simulações numéricas revelaram que os defletores frontais reduziram a transferência de calor em 21%, a operação com drive the velocidade variável a baixas velocidades diminuiu a transferência de calor entre 15% a 71%, e ventiladores menores causaram uma redução de 26%, enquanto alterações na tampa do fecho melhoraram a refrigeração em aproximadamente 6% e a remoção de até 24 tubos manteve a capacidade de refrigeração, sugerindo potencial de poupança de custos. No geral, o estudo avança na compreensão do comportamento térmico em motores com refrigeração por tubos e identifica parâmetros de projeto críticos para otimizar desempenho e sustentabilidade.

palavras-chave motor elétrico, transferência de calor, refrigeração a ar, analítico, dinâmica dos fluidos computacional

[1]Department of Mechanical Engineering (FEUP), Portugal. up202007496@up.pt
[2]Transport Phenomena Research Center, Department of Mechanical Engineering (FEUP), Porto, Portugal. aafonso@fe.up.pt

Introduction

Electric motors account for around 50% of global electricity consumption (Wierda & Zanutthi, 2024). In 2021, according to the International Energy Agency, electric motors accounted for around 70% of electricity demand in the industrial sector (International Energy Agency, 2021). The European Union (EU) has been regulating the energy efficiency of this equipment due to its environmental impact. All electric motors on the EU market have to comply with *Ecodesign* requirements and meet minimum efficiency levels (Stockton et al., 2024; Wierda & Zanutthi, 2024). In 2020, the 2019/1781 regulation covered 380 million motors, representing 56% of final electricity consumption in the EU (Wierda & Zanutthi, 2024).

The power delivered by a motor shaft is always lower than the input power, as part of the energy is lost and dissipated as heat, reducing efficiency below 100% (WEG S.A., 2024). These losses arise mainly from electrical resistance (Joule losses), magnetic effects, mechanical friction, and other secondary factors (Eletrobrás et al., 2009, Wang et al., 2022). In order to prevent them from reaching these limits, it is necessary to remove as much of the heat released by the motor as possible through an efficient cooling system. Motors can have closed or open systems. Among the closed systems, the most prevalent are air-to-air and air-to-water. The former are less efficient and noisier, but they are much simpler in construction and do not require care with used water (Gronwald & Kern, 2021; Nailen, 1975; Sung et al., 2021), and of objective of study in the present paper.

In the search for better solutions, these systems were studied through LPTN (Lumped Parameter Thermal Network) analysis, fast and less precise, and CFD, highly accurate, but at great computational cost (Ahmed et al., 2019). In the literature, it is possible to find some studies on motors or air-to-air heat exchangers.

A study on the cooling performance of a heat exchanger in a TEAAC motor and found that internally finned tubes improved heat transfer by 8.8%, lowered stator winding temperature by 4.1%, and reduced front motor surface temperature by 7.9 °C, despite causing a 3.4% decrease in external airflow due to higher pressure drop (Sung et al., 2021).

A high-capacity low-speed induction motor using a validated CFD model and found that an optimum number of cooling tubes reduces internal air temperature by 6.2°C, balancing improved heat transfer area with the drawback of increased air resistance (Yu & Meng, 2018).

Another study analysed the heat exchanger of a 500 kW high-voltage motor and showed that adding linear arc deflectors and optimizing baffles improves convective heat transfer, reduces vortices, and ensures a smoother, more uniform air velocity distribution in the tubes (Liu & Ai, 2022).

The baffle cute ratio is defined as the percentage of the shell diameter that is cut away in a segmental baffle to allow fluid flow in a shell-and-tube heat exchanger and to determine flow resistance and heat transfer performance. Baffle cute ratio of 30% provides the best balance between heat transfer and pressure drop, while removing tubes increases flow velocity and pressure drop but reduces residence time, degrading thermal performance. Overall, optimization of baffle number, cut ratio, and tube count is crucial to enhance heat transfer while minimizing excessive vortices and efficiency losses.

Through ANSYS Fluent, a study on a fin-and-tube heat exchanger found that increasing air mass flow rate (1–6 kg/s) enhanced heat transfer by boosting turbulence and reducing boundary layers (Tan et al., 2024). However, pressure drop rose exponentially, reaching 372 Pa at 6 kg/s, indicating significantly higher energy demands.

An article on a shell and tube heat exchanger using a program developed on the basis of theoretical formulas. They concluded that with a higher fluid flow rate it was possible to transfer more heat, but beyond a certain point the heat transferred remained practically constant (Azeez et al., 2024).

The cooling system that will the the scope of this study is the IC511. The IEC 60034-6 defines the cooling systems of electric motors with the letters IC (International Cooling), and the numbers indicate the types of ventilation. According to the standard, this system is characterized by a primary coolant, air in this case, that transfers its heat through a built-in heat exchanger, which ends up heating the surrounding medium, which serves as a secondary coolant. Also, it indicates that the coolants are moved by a fan mounted directly on the shaft (International Electrotechnical Commission (IEC), 2020). The system can be seen in Figure 1.

Figure 1 - IC511 refrigeration system.

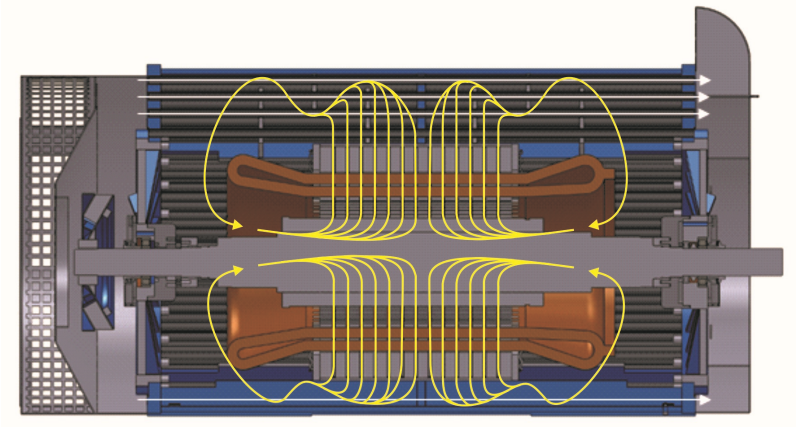

From "*Sizing of heat exchangers air-to-air in three-phase induction electric motors*" [Master's Thesis] by A. de Paula Ferreira, 2013.

As shown in Figure 1, the internal air circulates through two internal fans that pass through the radial channels of the stator and rotor, removing heat and rising to the tubes, constituting the phenomenon of external convection. Cooler ambient air enters through a grid, passes through a fan cover, which reduces noise, and is propelled by an axial fan that directs the air to the tubes with the help of the deflector cover, removing heat by internal convection. In situations of high noise production, a front air deflector can be used, as it is equipped with foam. This directs the air through a duct to the outside.

A study was conducted on enhancing internal heat transfer in an IC511 motor through CFD simulations in ANSYS Fluent, progressively using 2D, simplified 3D, and complete 3D models. The work revealed that rotor speed strongly influences airflow in the radial channels, with reduced speed leading to higher internal temperatures, particularly in regions distant from the air inlet. Hot spots were identified caused by poor airflow near the first rotor block and tested solutions such as flow guides, axial fan blade inversion, and stator casing modifications to improve cooling, achieving up to a 10°C reduction in internal air temperature. Furthermore, it was demonstrated that tube arrangement at a 30° angle enhanced turbulence and heat transfer, while selectively blocking initial radial channels improved airflow distribution and temperature uniformity in larger motors (de Paula Ferreira, 2013). Overall, this study provided key insights into internal airflow behavior and cooling performance.

From the literature review it is possible to observe that, although there are already some studies focused on improving heat transfer in air-to-air heat exchangers and in electric motors in general, there is a lack of specific studies on IC511 motors. On the other hand, the only thermal study found on this type of cooling system, focused only on the air circulation around the tubes without considering the internal convection within the tubes. This study therefore aims to analyse a motor with an IC511 system, focusing on heat transfer at the tube level and with the objective of understanding whether there is an air flow that maximizes heat transfer in the tube, which parameters are most influential and how flow configurations vary for different operating conditions and possible optimizations. First, an analytical model was developed to draw some initial insights, which allowed guiding the CFD simulations to study the most substantial operating conditions on heat transfer in the tubes. The two models were also combined to evaluate the thermal behavior in the whole tube system as explained later in the article.

Material and methods

Analytical model

For the analytical model, the study focused on a single pipe, neglecting housing to environment heat transfer in comparison to tube effects, as forced convection dominates over natural convection. Air temperature along the tube was assumed constant, enabling the use of the logarithmic temperature difference. Additionally, it was considered that all tubes contribute equally, with fan-driven airflow uniformly distributed and without recirculation.

An example of the type of tube under study is represented in Figure 2. The model input values were the inlet air temperature T_{in} (°C), the motor air temperature T_{∞} (°C), the tube length L (m), the mass flow rate $\dot{m}$ (kg/s), and the internal and external air convection coefficients h_i and h_o (W/m^{2}K), while the output was the outlet temperature T_{out} (°C), heat removed, and operational air speed for different conditions.

Figure 2 - Sketch of the tube under study.

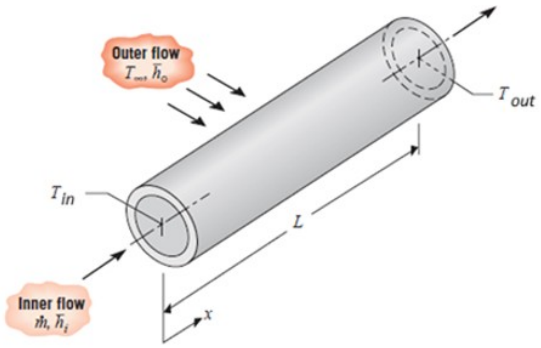

From "*Fundamentals of heat and mass transfer*" (7th ed.) by T. L. Bergman, A. S. Lavine, F. P. Incropera, & D. P. DeWitt, 2011, John Wiley & Sons.

The heat transfer phenomena occurring around the tube can be categorized into three distinct processes: external convection induced by the moving air generated by the internal fan, forced convection within the tube facilitated by the external fan, and conduction through the tube wall. Convection is the heat transfer between a surface and a moving fluid, characterized by the heat transfer coefficient ($h, W/m^2K$), estimated by Nusselt correlations. In equation (1), the Nusselt number (Nu) is calculated by the following expression (Bergman et al., 2011):

$$Nu = \frac{hL}{k_{air}}, \tag{1}$$

where, k_{air} is the fluid conductivity (W/mK).

Conduction refers to heat transfer within solids and fluids at rest, driven by molecular motion. All phenomena are represented through thermal resistances under steady state and unidirectional assumptions. In equation (2), thermal resistance is defined as (Bergman et al., 2011):

$$R = \frac{\Delta T}{\dot{q}}, \tag{2}$$

where, R is the thermal resistance (W/m^2K), ΔT is the temperature difference between the two media exchanging heat (ºC), and $\dot{q}$ is the heat flux being transferred (W/m^2).

External flow

External convection around a cylinder is described by the Hilpert correlation (Bergman et al., 2011), as shown in equation (3):

$$\overline{Nu_D} = CRe_D^m Pr^{1/3}, \quad Pr \geq 0.7, \tag{3}$$

where, $\overline{Nu_D}$ is the average Nusselt over the cylinder, C and m are empirical parameters, and Pr is the Prandtl number.

The Reynolds and Prandtl numbers are present in equation (4) and equation (5), respectively:

$$Re_D = \frac{\rho V D_{ext}}{\mu}, \tag{4}$$

and

$$Pr = \frac{\mu c_p}{k_{air}}, \tag{5}$$

where, ρ is the air density (kg/m^3), V is the air velocity (m/s), D_{ext} is the outer diameter of the tube (m), μ is the air viscosity (Pas) and c_p is the air specific heat (J/kgK).

The properties of the fluid should be assessed at the ambient air temperature surrounding the pipe within the motor. In regard of air speed measurement, direct assessment within the motor is unfeasible. The values used in this work were derived from two-dimensional simulations conducted by de Paula Ferreira (2013).

Conduction

In the context of the tube problem, heat transfer takes place through the thickness of the tube. The thermal resistance associated with conduction is (Bergman et al., 2011), as shown in equation (6):

$$R_{cond} = \frac{\ln\left(\frac{r_2}{r_1}\right)}{2\pi L k_{tube}}, \tag{6}$$

where, r_1 is the tube inner diameter (m), r_2 is the tube radius outer diameter (m), k_{tube} is the tube material conductivity (W/m^2K).

Inner flow

For fully developed laminar flow, the Nusselt number is $Nu = 3.66$ (constant wall temperature). For turbulent flow ($Re \geq 10000$), the Dittus-Boelter correlation was used (Bergman et al., 2011), as shown in equation (7):

$$Nu_D = 0.023 Re_D^{4/5} Pr^{0.4} \quad (0.6 \leq Pr \leq 160,\ L/D \geq 10). \tag{7}$$

For the transition regime, the Gnielinski correlation was applied (Bergman et al., 2011), as shown in equation (8):

$$Nu_D = \frac{(f/8)(Re_D - 1000)Pr}{1 + 12.7(f/8)^{1/2}(Pr^{2/3} - 1)} \quad (0.5 \leq Pr \leq 2000,\ 3000 \leq Re \leq 5 \times 10^6). \tag{8}$$

The properties of air must be assessed at the average temperature established between inlet and outlet. Therefore, this necessitates an iterative calculation process, as the outlet temperature is initially indeterminate. Consequently, the code must be initialized with an estimated value until convergence is achieved in accordance with a predefined error threshold. The problem is characterized by three thermal resistances connected in series: external convection, internal convection, and conduction. A schematic representation of the resistances model is provided in Figure 3.

Figure 3 - Thermal resistances in series.

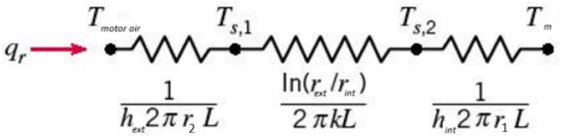

From "*Fundamentals of heat and mass transfer*" (7th ed.) by T. L. Bergman, A. S. Lavine, F. P. Incropera, & D. P. DeWitt, 2011, John Wiley & Sons.

The total resistance is then the sum of the three resistances, as:

$$\frac{1}{UA_{ext}} = \frac{1}{h_{ext}A_{ext}} + R_{cond} + \frac{1}{h_{int}A_{int}}, \tag{9}$$

where U is the global heat transfer coefficient (W/m^2K), R_{cond} is the conductive resistance (W/m^2K), mh_{ext} (h_o) and h_{int} (h_i) denote the external and internal heat transfer coefficients, respectively $(W/m, K)$, while A_{ext} and A_{int} represent the external and internal tube surface areas, respectively (m^2).

The logarithmic temperature difference (ΔT_{mL}) is given in the following equation (10):

$$\Delta T_{mL} = \frac{T_{out} - T_{in}}{\ln\left(\frac{T_{ma} - T_{in}}{T_{ma} - T_{out}}\right)}, \tag{10}$$

where, T_{ma} (T_∞) is the motor air temperature (ºC).

The ultimate equation that addresses the problem is derived by equating the heat transferred through the tube:

$$\dot{Q} = UA_{ext}\Delta T_{mL}, \tag{11}$$

with the heat absorbed by the air within the tube, as determined by the first law of thermodynamics:

$$\dot{Q} = \dot{m}c_p(T_{out} - T_{in}), \tag{12}$$

where, $\dot{m}$ is the air mass flow rate in the tube (kg/s).

To carry out the analysis, it is essential to assess the pressure losses that occur within the pipes. These losses can be categorized into two types: in-line and local. In-line pressure losses can be calculated using the following equation (13) (Munson et al., 2012):

$$\Delta p = f\frac{L}{D}\rho\frac{V^2}{2}, \tag{13}$$

where, Δp is the tube in-line pressure loss (Pa), f is the Darcy friction factor and V is the air velocity in the tube (m/s).

The Darcy friction factor depends on whether the flow is laminar, turbulent, or transitional. For laminar flow, the following equation (14) is used:

$$f = \frac{64}{Re}. \tag{14}$$

The Petukhov formula associated with the Gnielinski equation (15) shown above can also be used for a range of Re that encompasses both the transition and turbulent regimes:

$$f = (0.79\ln(Re_D) - 1.64)^{-2}. \tag{15}$$

For the turbulent regime, the Blasius equation (16) ($Re \leq 500000$) for smooth tubes was used, due to its simplicity and applicability to the tube:

$$f = \frac{0.316}{Re^{1/4}}. \tag{16}$$

Local losses are calculated using the following equation (17):

$$\Delta p = K_L\frac{1}{2}\rho V^2. \tag{17}$$

Local losses in the pipe are the losses at the inlet and outlet of the pipe. The local loss coefficient (K_L, dimensionless) in the first case is0.5 and 1 in the second (Munson et al., 2012).

The tube under analysis has a diameter of 28 mm, a thickness of 1 mm, and a length defined by the motor casing. Model inputs include the inlet air temperature (–20°C to 40°C) and the surrounding motor air temperature (inlet temperature plus 80K, overheating limit considering B electrical insulation class). The model was solved iteratively using Engineering Equation Solver (EES) and serves two main purposes. Firstly, to identify the optimal air velocity that would maximize tube heat transfer, providing a benchmark for testing and enabling the detection of possible recirculation or design issues. Secondly, to evaluate the influence of parameters such as fan speed, fan type, tube length, and diameter, thereby identifying the most significant factors for more detailed numerical assessments.

Numerical model

Computational Fluid Dynamics (CFD) uses numerical methods to approximate solutions of the Navier–Stokes equations, ensuring conservation of mass, momentum, and energy to predict fluid behavior and heat transfer. Integrated with CAE software and validated against experimental data, CFD is particularly valuable for evaluating performance variables when laboratory testing is costly, complex, or unsafe (Raman et al., 2018). In this section, the governing equations and considerations behind the numerical study are presented.

Governing equations

The conservation of mass (m) represented by Lagrange is given by equation (18):

$$m = \rho Vol = \text{const}, \tag{18}$$

where ρ is the fluid density and Vol is the particle volume.

Applying the material derivative presented above, we obtain the continuity equation in its general form, as shown in equation (19):

$$\frac{\partial \rho}{\partial t} + \nabla \cdot (\rho \mathbf{V}) = 0, \tag{19}$$

where $\mathbf{V}$ is the fluid velocity vector. In the presence of incompressible flow, the density does not vary with time or space, and as such the equation only reduces to the divergence of the velocity vector equal to zero, implying that the particles have a constant volume (White, 2006).

According to Newton's second law, the force applied is equal to the mass times the acceleration. In fluid mechanics, density is used instead of mass, and the applied forces are broken down into body and surface forces. Body forces are those that apply to the mass of the fluid element, such as gravity, while surface forces are due to external forces applied to the sides of the element. Thus, Newton's law becomes the Navier-Stokes law (White, 2006):

$$\rho \frac{D\mathbf{V}}{Dt} = \rho \mathbf{g} - \nabla p + \frac{\partial}{\partial x_j} \left[\mu \left(\frac{\partial v_i}{\partial x_j} + \frac{\partial v_j}{\partial x_i} \right) + \delta_{ij} \lambda \operatorname{div} \mathbf{V} \right]. \tag{20}$$

Most engineering flows are turbulent, marked by instability, three-dimensionality, vorticity, and stochastic behavior, though they also contain coherent structures that reoccur periodically. To predict these flows and improve design efficiency, engineers rely on models such as Direct Numerical Simulation (DNS), Reynolds-averaged Navier-Stokes (RANS), and Large Eddy Simulation (LES) (Wilcox, 2006). The RANS equations are extensively utilized within the field of computational fluid mechanics and are employed in this thesis as well. Various quantities associated with turbulent flow can be characterized by an average value ($\overline{u}_i(\mathbf{x}, t)$) along with the instantaneous fluctuations ($u_i'(\mathbf{x}, t)$) related to that average, as shown in equation (21):

$$u_i(\mathbf{x}, t) = \overline{u}_i(\mathbf{x}, t) + u_i'(\mathbf{x}, t). \tag{21}$$

Therefore, the speed of the *i* component depends on its position *x* and time *t*. This representation of quantities is incorporated into the Navier-Stokes equations, and through the application of time averaging, the Reynolds-averaged Navier-Stokes (RANS) equations are derived, which are subsequently solved for the averaged quantities. These give rise to new variables such as the term $\overline{\rho u_i' u_j'}$, better known as the Reynolds stress tensor. To address the challenge at hand, it becomes evident that new equations are necessary, leading to the development of turbulence models. Among these, eddy viscosity models are the most prevalent. They propose that turbulence is characterized by small eddies and are grounded in the Boussinesq hypothesis. These models assume that the Reynolds stresses are influenced by the strain rate and the concept of eddy viscosity, μ_t. The representation of the stress tensor is as follows in equation (22):

$$-\overline{\rho u_i' u_j'} = \mu_t \left(\frac{\partial \overline{u}_i}{\partial x_j} + \frac{\partial \overline{u}_j}{\partial x_i} \right) - \frac{2}{3} \delta_{ij} \left(\rho k + \mu \frac{\partial \overline{u}_l}{\partial x_l} \right), \tag{22}$$

where, *k* is the turbulent kinetic energy:

$$k = \frac{1}{2} \overline{u_i' u_i'}. \tag{23}$$

The issue at hand has shifted from addressing Reynolds stresses to accurately modeling eddy viscosity. Among the various approaches, two-equation models are preferred for their balance between precision and computational efficiency. The velocity and length scale are addressed through individual transport equations. These models fall into two categories: the $k-\omega$ model and the $k-\epsilon$ model. There are different $k-\omega$ models such as Wilcox, Baseline (BSL), and the most popular, the Shear Stress Transport (SST) model. The $k-\omega$ - SST model factors in the transport of turbulent shear stress, which allows for highly accurate predictions. In contrast, other models like BSL overlook this transport, leading to an overestimation of the eddy viscosity.

To achieve the right outcomes, it is essential to limit the eddy viscosity accordingly. The effectiveness of the method relies on the integration of blending functions, which are formulated based on the proximity of the nearest surface to the flow variables. Consequently, when employing this model, CFX tracks the Wall Scale equation to facilitate the blending process between the $k-\epsilon$ and $k-\omega$ models (ANSYS, 2021b).

Geometry

Simulations were conducted both with and without the front air deflector, leading to six air domains in the former scenario and seven air domains in the latter. Figure 4 illustrates the different domains and their connections.

Figure 4 - Simulation air domains.

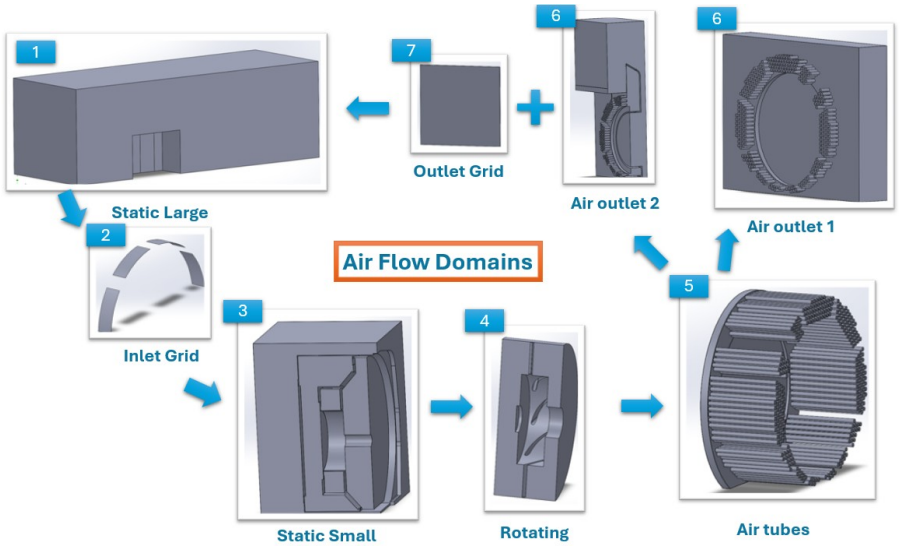

The blue arrows indicate the direction of air circulation. A summary of the different sections and their functions is provided below:

- **D1 - Static Large**: represents the box with still air in the large area surrounding the motor, representing the room where the motor is placed;
- **D2 - Inlet Grid**: simulates the effect of the grid on the passage of air;
- **D3 - Static Small**: allows for greater refinement with smaller element sizes when approaching the motor;
- **D4 - Rotating**: replicates the impact of the rotation of the fan on the surrounding air, which consequently influences the static domains by drawing in and expelling air;
- **D5 - Air Tubes**: air entering through the pipes and circulating to the outlet;
- **D6 - Air Outlet 1**: unobstructed air outlet to the outside environment;
- **D6/D7 - Air Outlet 1**: air outlet to the front air deflector, commonly used by WEG for high-speed motors, with the addition of the grid through which the air passes to the outlet.

The large static domain (D1) is wide enough and long enough to avoid influencing the flow around the motor. If care is not taken with the size of the larger domain and the outlet zone is close to the air outlet of the pipes, recirculation may occur, causing inflow at the outlet (ANSYS, 2021a). The simulation provides a modular capability, allowing for the connection of both options to the outlet of the tubes, contingent upon the inclusion or not of the front deflector.

Mesh

The mesh, created in ANSYS, was validated through a mesh independence test to ensure accuracy and quantify the numerical error of the model. The mesh convergence test assesses discretization error in CFD, where finer meshes reduce error but increase computational cost. To balance accuracy and efficiency, the numerical error of coarser meshes must be quantified, which in this work was done using Richardson's extrapolation (Nasa Glenn Research Center, 2021). The method enables the estimation of the continuous value at zero grid spacing. Equation (17) employed in its generalized form is as follows:

$$f_{h=0} \approx f_1 + \frac{f_1 - f_2}{r^p - 1}, \tag{24}$$

where, $f_{h=0}$ is the value at zero grid spacing, f_1 and f_2 are the values for the finer grids, r is grid refinement ratio and p is the order of the method. For this study, a grid refinement ratio of two was considered ($r = 2$), meaning that meshes were tested successively by doubling the number of elements from the coarsest to the finest, and a second-order approximation was used ($p = 2$). The meshes of the different domains are shown in Figure 5.

Figure 5 - Calculation mesh.

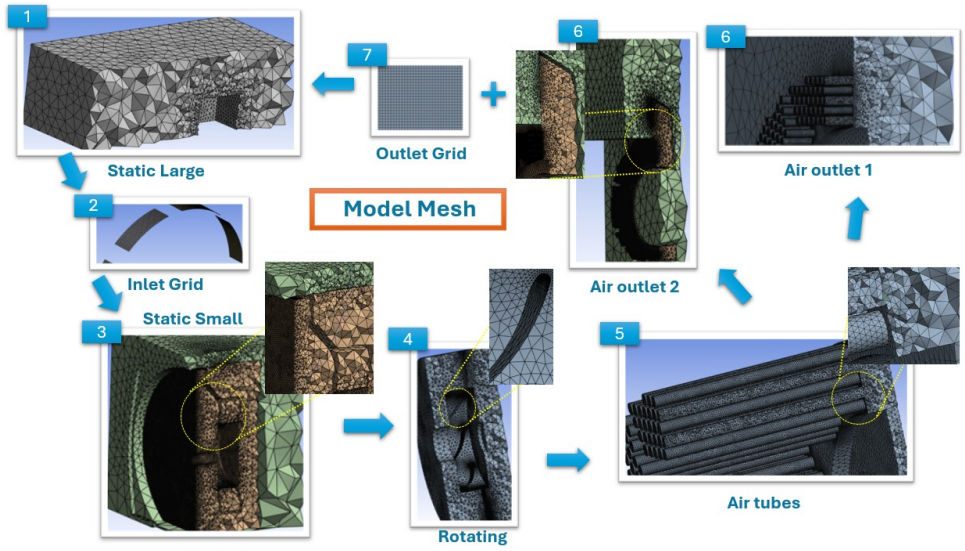

The complexity of the mesh represented in Figure 5 is evident, particularly within the constraints of the small static domain, which can be attributed to the inherent geometry. Specifically, the mesh configuration in regions adjacent to the walls, including areas in contact with the deflector cover and the blade in the rotating domain, as well as near the tubes in the air-tube domain and in contact with the final deflector, can be observed in detail.

Results and discussion

Analytical results

The initial series of calculations was conducted with an external air temperature of 20°C and a fixed internal motor temperature of 100°C. The objective was to study how the heat removal capacity of the tube changes with the velocity of the airflow passing through it. The heat removal is presented in Figure 6.

As illustrated in Figure 6, the heat removal follows a logarithmic type of evolution. It is important to highlight that the speeds at which the air would not be able to heat properly remain significantly elevated, more than 150 m/s. This conclusion is in line with the study of Abu et al. (Azeez et al., 2024), in which heat transfer also ceases to increase with higher fluid flow rates, even for other geometric configurations. Based experimental results gathered from experimental prototype tests, the air speeds and the temperatures of the air at the outlets of two pipes were registered and are present in Table 1.

Figure 6 - Heat removed by the tube (Q) as a function of air velocity (v int) for T_{in} = 20ºC and T_{motor} = 100ºC.

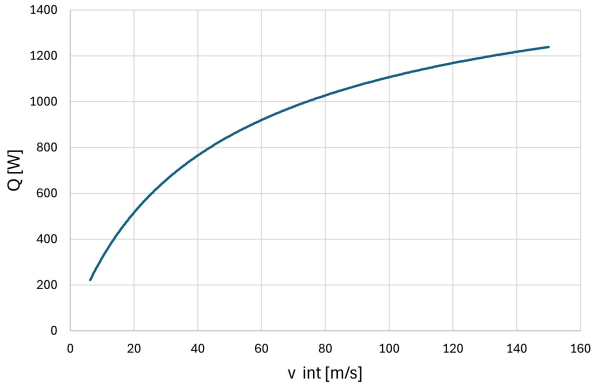

Table 1 - Experimental measurements in two tubes.

Tube	(m/s)		(ºC)	
	v_{exp}	v_{mean}	T_{in}	T_{out}
1	9.3	7.6	23.6	54.5
2	18.51	15.2	23.6	95.2

In Table 1, v_{exp} is the experimental velocity measured at the centre of the tube, v_{mean} is the mean velocity in the tube obtained by dividing the axis speed by 1.22 for turbulent flow (White, 2006). T_{in} is the inlet temperature and T_{out} is outlet temperature of tube air. Based on the analysis of the involved speeds, it can be ascertained that the air undergoes significant heating, achieving temperature jumps of 31°C and 72°C, respectively. Also, these speeds are still well below the value at which air would be unable to heat adequately due to low residence time. Consequently, it is reasonable to deduce that there is no singular optimal speed that maximizes heat transfer within the pipes. Instead, it is evident that, for motors actual conditions, the air velocity can be increased without concern of being so high that the air stops heating properly. The evolution of pressure drop with air speed has an exponential relation as expected, shown in Figure 7.

Figure 7 - Pressure losses in the tube (Delta P) as a function of air velocity (v int) for T_{in} = 20°C and T_{motor} = 100°C.

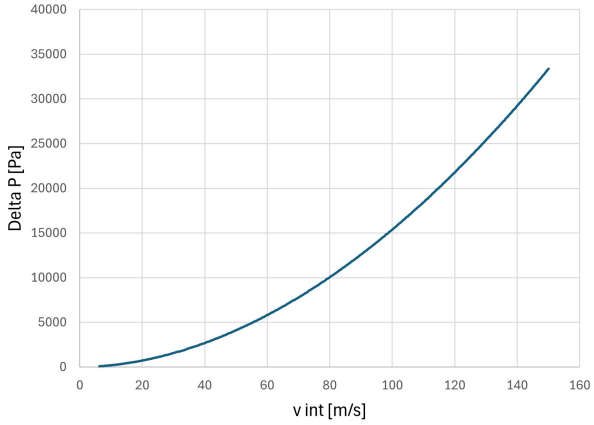

In order to study how different parameters affect heat transfer capacity, a limit to pressure drop must be defined. It was defined that the capacity of the fan in use to overcome the pressure drop associated with the tube was the limit. Subsequently, in order to assess the operational velocities within the tubes it was necessary to consider the use of total pressure curves in relation to the volumetric flow rates for different axial fan diameters and rotation speeds, taken from a supplier catalog (Soler & Palau Ventilation Group, 2025). Figure 8 illustrates where the tube pressure drop curve (depicted in dark blue) intersects with the head flow rate curves corresponding to three fans with different diameters, for 3450 RPM.

This intersection point represents the operating point inside the tubes that allows the fan in question to remove as much heat as possible. Knowing the operation speed, it was possible to determine the heat removed by the tube for each situation, since the pressure losses curve varies for different parameters under study. For this initial case, the values obtained are shown in Table 2.

Figure 8 - Intersection of tube pressure loss curve with fan curve.

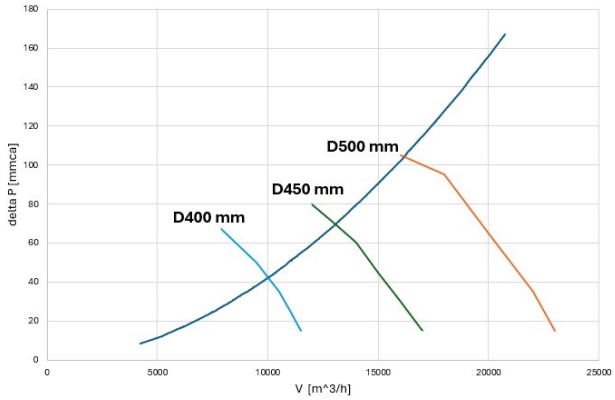

Table 2 - Results obtained for initial case.

Fan Diameter (mm)	**500**	**450**	**400**
v (m/s)	23.9	20	15.1
Re	39433	33179	24511
$\dot{m}$ (kg/s)	0.01651	0.01393	0.01034
$\dot{Q}$ (W)	572	516	425
$\dot{Q}$ total (W)	173766	156803	129322

Fan diameter

The impact of employing a fan with a smaller diameter is evident, as this design choice leads to a decrease in the velocity of the air within the tubes, resulting in a reduced capacity for heat removal. The total heat removal is determined by multiplying the heat removed by an individual tube by the total number of tubes in operation, 304. This calculated value represents the theoretical maximum potential for heat dissipation achievable by the tube system, and it also indicates the upper limit of joule losses that the stator and rotor of the motor can endure. Beginning with this initial case, the impact of various parameters on heat transfer was examined by systematically altering each parameter in sequence.

Tube length

The variation in tube length fundamentally impacts the heat transfer area, thus, an increase in tube length corresponds to an enhancement in the amount of heat transferred. Reducing the value to 1935 mm results in an impact of 3.7%, whereas increasing it to 2135 mm yields an impact of 2.1%, Table 3.

Table 3 - Tube length variation.

L (mm)	**1935**	**2035**	**2135**
v (m/s)	20.1	20	19.9
$\dot{Q}$ (W)	497	516	527

Tube thickness and material

As with the length, increasing the thickness outwards increases the heat transfer area. The impact of increasing to 5 mm is 3.1% and to 10 mm is 6%, Table 4.

A thickness of 10 mm was evaluated to ascertain that, even at this elevated value, the influence of conduction resistance remains minimal, contributing only 2.2% to the total thermal resistance.

Table 4 - Tube thickness influence.

e (mm)	**1**	**5**	**10**
$v\ (m/s)$	20	20	20
$\dot{Q}\ (W)$	516	532	547

Therefore, it can be concluded that provided the tube material is not a thermal insulator, there is no significant impact on heat transfer. Increasing the thickness of the pipe towards the interior increases the pressure drop while simultaneously decreasing the volumetric flow rate through the pipe. This alteration, when translated to velocity, yields a higher value. However, a reduction in diameter significantly affects the mass flow rate, as this is proportional to the square of the diameter; consequently, the heat transfer within the pipe is adversely affected. For 2 mm the decrease is of 6.8% and for 4 mm, none of the fans could support the pressure drop, as the curves did not intersect, Table 5.

Table 5 - Increase tube thickness in inner direction influence.

e_i (mm)	**1**	**2**	**4**
$v\ (m/s)$	20	20.3	-
$\dot{Q}\ (W)$	516	481	-

Motor and ambient air temperature

As expected, when operating at lower temperatures, the tube has better thermal performance than when operating at higher temperatures. The increase in temperatures yields a decrease in heat transfer of 2.1% and 4.1%. On the other hand, the decrease in temperatures results in increases in heat transfer of 0.97%, 3.3%, 5.8%, and 8.3%, Table 6.

Table 6 - Temperatures influence.

$\mathbf{T}_{motor}$ (°C)	$\mathbf{T}_{amb}$ (°C)	$\mathbf{v}\ (m/s)$	$\dot{\mathbf{Q}}\ (W)$
20	100	20	516
-20	60	20	559
-10	70	20	546
0	80	20	533
10	90	20	521
30	110	20	505
40	120	20	495

Rotation speed influence

When operating with a Variable Speed Drive (VSD), the motor can operate at variable rotation speed. For a motor where the reference frequency is 50 Hz, it can be as low as 5 Hz, which corresponds to a range of rotation speeds from 300 to 3000 RPM. As the supplier had curves for 850, 1150 and 1750 RPM, it was possible to extrapolate the results to the range mentioned, Table 7.

Table 7 - Thermal behavior with changing rotation speed.

RPM	**300**	**600**	**1200**	**1800**	**2400**	**3000**
$v\ (m/s)$	-	1.4	7.3	11.8	14.9	16.5
$\dot{Q}\ (W)$	-	83	240	353	423	450

It is important to note that as operational speeds decrease, the efficacy of heat transfer is significantly diminished, specifically, there are reductions of 6%, 22%, 47% and 82% when compared to the performance at 3000 RPM. At 300 RPM, it can be observed that the tube fails to effectively remove heat, while at 600 RPM, the tube operates in the transition regime. It should be noted that for this calculation, the air speed around the tube was also varied, according to the study on the same type of motor mentioned in the literature review, successively reducing as the rotation speed was lowered.

Summary

The semi-analytical study showed that fan speed and diameter, through their effect on air velocity, are the most influential parameters for heat transfer, outweighing tube geometry or operating temperatures. This guided the continuation of the work with CFD simulations focused on determining flow configurations for different operating conditions, namely for fan and rotation speed, as they were the most influential.

Numerical results

This section presents the different results obtained by simulation and their connection to the analytical thermal models, for different operating conditions. The numerical simulations were performed for the air flow only in isothermal conditions.

Mesh independence test

The first step was to run the model for three different meshes and observe the variation in error with consecutive refinement, as mentioned above. The error was determined by evaluating a flow variable between the mesh used and the the situation which infinity elements (Infinity M) would be used, calculated by the Richard's extrapolation. Figure 9 shows the results.

Figure 9 - Mesh independence test.

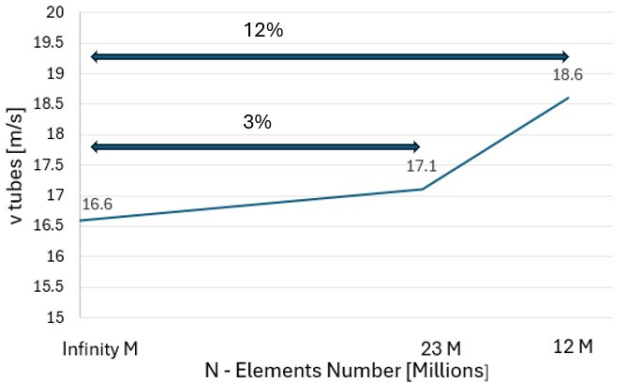

The variable considered for the mesh study was the average outlet velocity in the cooling system pipes. The 6 million element mesh showed non-monotonic behavior in some pipes and, as such, was considered to be outside of the convergence radius. The remaining two meshes indicate that the more refined mesh allows for a smaller error compared to the infinite refinement solution. The choice of mesh to use must be a compromise between computational cost and the numerical error associated with the model. The 12 million element mesh has that compromise, as it has an acceptable error and a much shorter simulation time than the 23 million mesh (more than 24 hours compared to only 8 hours).

Validation with experimental results

It is imperative to compare the model with the results obtained from experimental tests to ascertain that the baseline case, from which various comparisons for differing conditions will be derived, approximately reflects real behavior. Consequently, the simulation was conducted utilizing a 500 mm fan operating at a rotational speed of 3000 RPM, the same conditions of experimental tests. As already mentioned, a shorter pipe length was used than in reality, so the values read from the pipes in the simulation will always be higher

than the experimental ones. As the pressure drop that the fluid must overcome being simulated is lower than in reality, more air flows through the pipes. A comparison was conducted between the experimentally recorded average speed and the average speed derived from the numerical model at the same points, as shown in Table 8, and an error of only 12.2% was calculated.

Table 8 - Experimental Validation.

Parameter	**Value**
Medium Velocity Experimental (m/s)	19.33
Medium Velocity Model (m/s)	17.23
Error (%)	12.2

It is important to highlight that the general behavior of the various tubes, regarding the distribution of air flow, aligns with the experimental findings observed in each measured tube sector.

Base case - fan diameter 500 mm and 3000 RPM

Figure 10 shows the contour of the air distribution throughout the tube for a fan diameter of 500 mm and 3000 RPM.

Figure 10 - Air distribution throughout the tubes for a fan diameter of 500 mm and 3000 RPM.

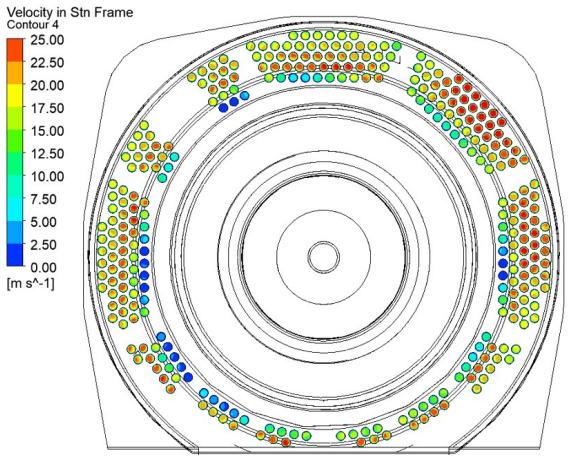

Air circulation in the inner tubes near the endshield is restricted due to the wall, reducing airflow compared to other tubes, while the bottom geometry of the motor and the clockwise fan rotation further create an uneven velocity distribution, with the top-right sector receiving the highest flow, as also confirmed experimentally. However, velocity alone is insufficient to assess heat transfer, since tubes closer to the motor center are exposed to warmer air, making it essential to estimate heat removal from each tube to fully understand thermal behavior under different operating conditions. To address this, the analytical model that assumes a constant air temperature surrounding the tube was considered, serving as a preliminary approach.

Given the limited data regarding the internal temperatures of the motor, it became our responsibility to define the thermal load. Nonetheless, this approach remains satisfactory for extrapolating behavior under different scenarios. However, it should be noted that all conclusions drawn about thermal behavior are inherent to the load prescribed here, and may differ for other loads. Firstly, it was considered constant radial temperatures that decrease from the innermost radius (r_1) to the outermost radius (r_6) of the tubes, as seen in Figure 11.

Figure 11 - Radial variation of motor air temperature across the tubes assumed, considering $r = r_i$, $i = 1, ..., 6$.

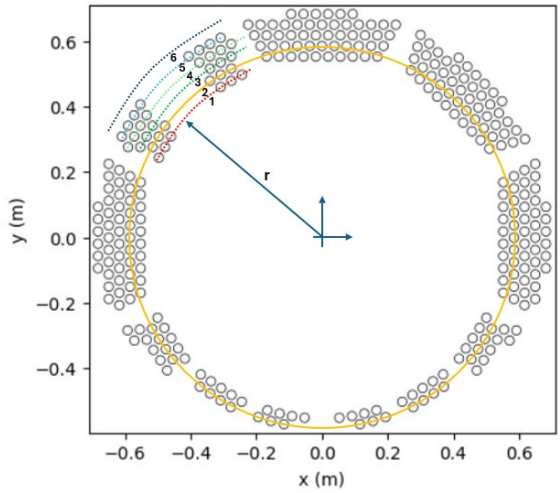

The temperature at the innermost radius (r_1) was established at 105°C, derived from the sum of 25°C (representing the air temperature in the simulations) and 80°C (reflecting the aforementioned temperature differential). The trend was modeled by the following equation (18):

$$T(r) = T_{r_{ext}} + (105 - T_{r_{ext}}) \left(1 - \left(\frac{r}{r_{\max}}\right)^n\right), \tag{25}$$

where, $T_{r_{ext}}$ is the outer radius temperature (°C), r is the radius of each circle shown above (m), r_{max} is the outer radius (m) and n is the parameter that models the curve form. The $T_{r_{ext}}$ was given an initial value of 60°C and it was afterwards studied its effect. The value of n was assigned as fifteen, as this resulted in a slight reduction of the air motor temperature in the first three initial radius, with a more significant decrease observed in the outer three radius.

With the specified temperatures surrounding the pipes, inlet temperature and the average velocities obtained from each pipe in the simulation, the analytical model, shown above, was employed to forecast the thermal behavior of each pipe. The EES model receives, for each tube, the local medium air velocity and the corresponding air motor temperature based on its spatial position. It then solves the governing equations individually for each tube to determine its respective thermal contribution. To improve the visual presentation of these results, a *Python* script was developed to generate an image illustrating the tube arrangement together with the computed values, represented using an appropriate color scale. The resulting image for this initial simulation is shown in Figure 12.

Figure 12 - Heat absorbed by each tube ($T_{r_{ext}}$ =60°C) for 500 mm and 3000 RPM.

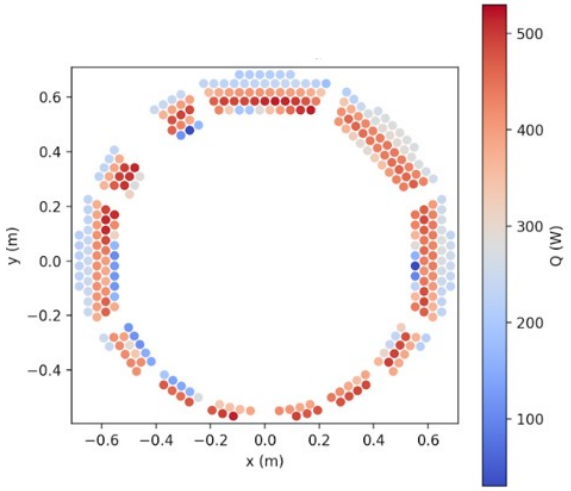

As anticipated, some tubes situated near the wall, where air circulation is limited, exhibit a decreased capacity for heat removal, despite their location in the hottest zone. Furthermore, it is imperative to emphasize that the peripheral tubes, although exposed to a greater quantity of air, such as the ones at the right-hand top corner, ultimately extract less heat when compared to other tubes. This phenomenon occurs because these peripheral tubes are located in areas surrounded by cooler air. Commencing from this point, an analogous study was conducted under varying operational conditions and comparisons in percentages were made to this base case.

Use of front air deflector

In Figure 13 it is possible to see the damaging effect on air reaching the tubes because of this element. The zones A, B, C, and D represent tube sectors that are highlighted in order to observe the effect.

Figure 13 - Front air deflector effect on air circulation: (a) without front air deflector, (b) with front air deflector.

(a) (b)

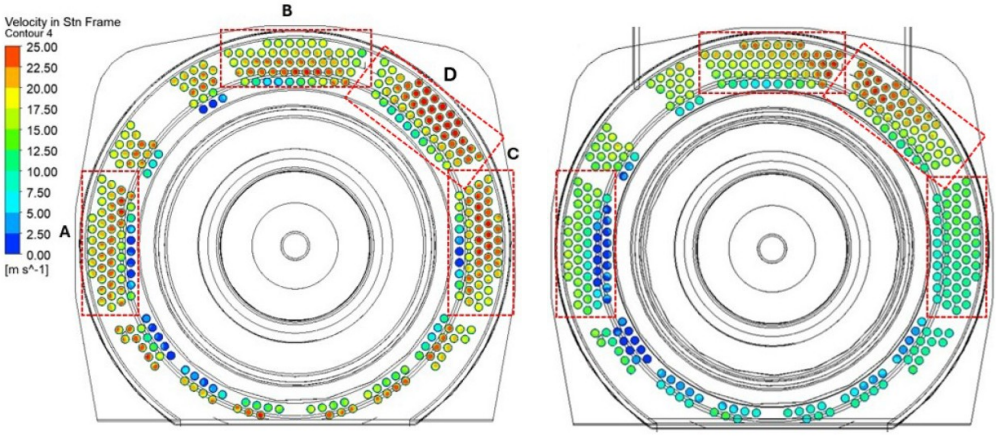

The pipes situated at the lower and lateral sections are adversely affected, as the air must navigate through a more constricted segment of the deflector. This configuration results in an additional pressure drop, inadvertently diverting air from these regions. Conversely, the air within the upper tubes tends to escape into a less confined area of the deflector, thereby mitigating potential damage. This effect is well represented by the vector plot in Figure 14.

Figure 14 - Vector plot of the front air deflector effect.

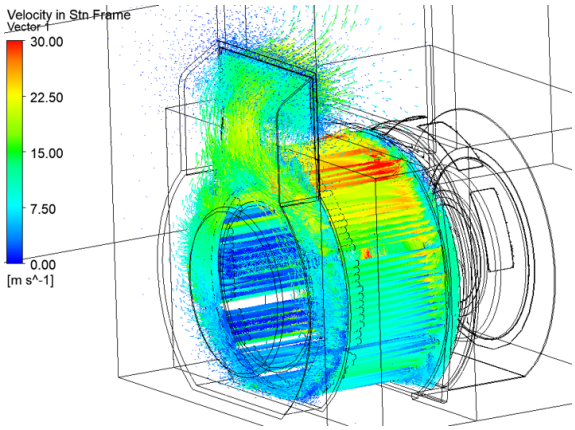

Furthermore, it is noteworthy that the front deflector partially overlaps certain downpipes, which also explains its negative effect in these areas. In Table 9 the following air reductions occur in the four sections (A, B, C and D).

Table 9 - Air speed reduction in the different areas.

Mean air speed (m/s)	Without front deflector	With front deflector	Correction Factor
A	17.88	10.35	0.58
B	17.97	18.5	1.03
C	18.59	11.27	0.61
D	20.95	19.2	0.92

In Figure 15 it is possible to observe the negative impact on heat removal. The percentages indicate the overall heat transfer loss (top left) and the losses by zone (A, C and pipes below).

Figure 15 - Front air deflector influence on heat removal (heat absorbed - with front air deflector).

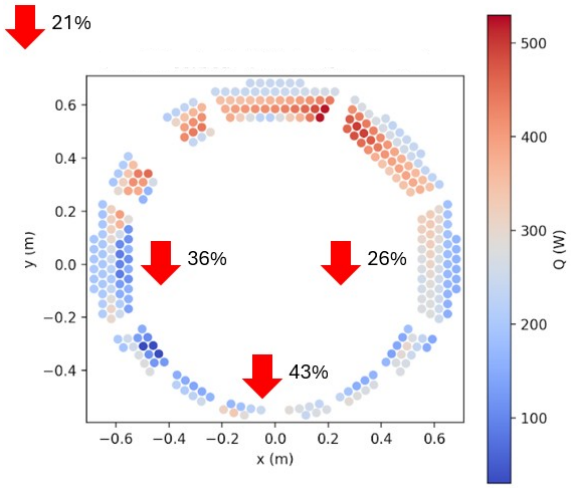

The lower area has been significantly impacted and the overall loss is also significant. Consequently, regarding heat transfer, it is advisable to minimize the use of this deflector, reserving it only for circumstances of extreme noise. Additionally, the hot air emitted from the pipes typically does not pose an issue for the machine of the customer, as it operates at a higher temperature.

Fan rotation speed effect

Motors are largely driven by VSD (Variable Speed Drive), which means that the customer can run the motor at different frequencies depending on their needs. The frequency can be as low as 10% of the network frequency, usually 50 or 60Hz. The previous simulation considered 50Hz and now the frequencies have been varied to 40, 30, 20 and 10Hz. Figure 16 shows the variation in the air received by the tubes as the rotation speed varies.

The analysis of the flow configuration reveals that the distribution is preserved by examining the tubes that receive more or less air. However, as anticipated, the mean velocity values exhibit a substantial decrease, as illustrated in the Table 10. The correlation between the average airspeed and the rotational speed can be represented by a linear relationship ($V_{mean} = 0.0061$ RPM-0.13).

The heat transfer loss compared to the situation with the fan running at 3000 RPM is shown in the Figure 17.

The evolution of heat transferred for different rotation speeds can be described by a quadratic relationship ($\dot{Q} = -0.0031$ RPM$^2 + 42.6$ RPM $+ 5814.4$). These simulations also showed periodic oscillations in the speed monitors of sector B only. Calculation of the Strouhal ($\approx 10^{-4}$), in equation (26) number reveals that these may be high-scale recirculations arising from the fact that the flow is weaker than at 3000 RPM,

$$St = \frac{fL}{D}, \tag{26}$$

where, the quantities f, L and V represent the specific frequency (Hz), length (m), and velocity (m/s) scales that effectively characterize the unsteady behavior of the problem being studied.

Figure 16 - Effect of rotation speed in the airflow: (a) 2400 RPM (40 Hz), (b) 1800 RPM (30 Hz), (c) 1200 RPM (20 Hz), and (d) 600 RPM (10 Hz).

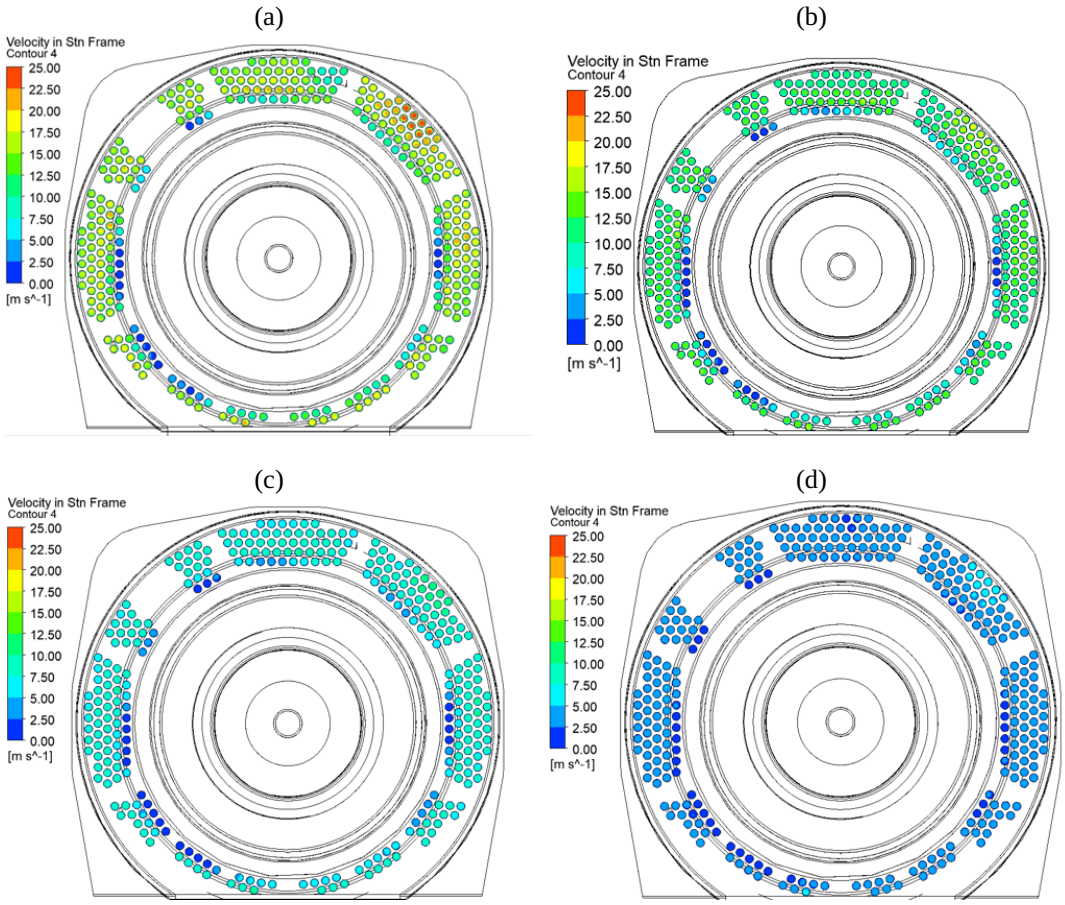

Table 10 - Mean air speed across the tubes for different RPM.

RPM	V_{mean} **(**m/s**)**
3000	18.1
2400	14.5
1800	10.8
1200	7.2
600	3.5

The concept of the Strouhal number was developed to address the dynamics of periodic fluid flows (Trivellato & Raciti Castelli, 2015). The frequency was determined by the inverse of the number of time-steps between oscillations, the length was defined as the diameter of the fan, and the speed was considered as the peripheral velocity of the fan.

As studied numerically by Louw et al. (2014), as the flow-rate that goes through the fan decreases, the re-circulations appear. Although, at 600 RPM, the oscillations stop appearing again.

Fan diameter effect

This two-polarity motor usually uses three axial fans of different diameters, 400, 450 and 500 mm. To assess the influence of adopting smaller-diameter fans, which modify the flow configuration and, consequently, the resulting thermal behavior. The deflector cover remains the same for these fans, only changing the internal air deflector that changes to a smaller diameter to accommodate the 450 and 400 fans.

Figure 17 - Effect of rotation speed in the heat absorbed: (a) 2400 RPM, (b) 1800 RPM, (c) 1200 RPM, and (d) 600 RPM.

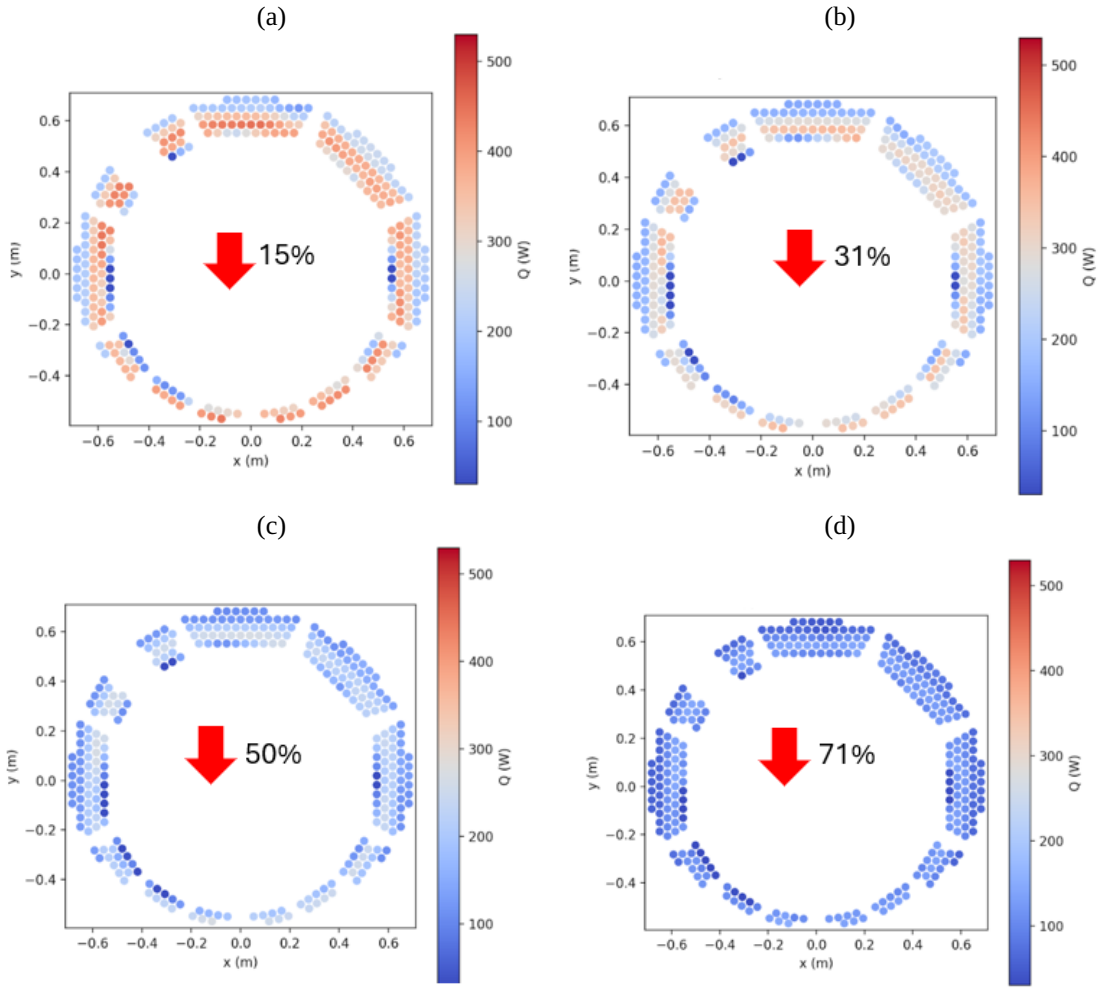

In contrast to the 500 mm simulation, both the 450 mm and 400 mm simulations exhibited periodic oscillations across all monitors. This observation supports the conclusion that the fluid flow is significantly more unstable and diminished in strength with the fan replacement. The air distributions are present in Figure 18.

Figure 18 - Fan diameter flow rate effect: (a) 450 mm, and (b) 400 mm.

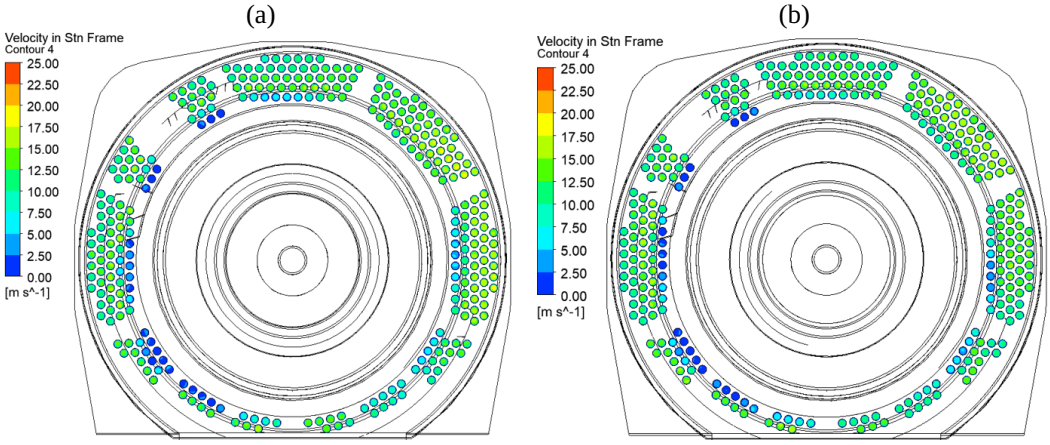

Due to fluctuations in all monitors, the average speeds of each monitor were determined and the overall average of these values was calculated for each case. The values are presented in the following Table 11.

Table 11 - Mean air speed across the simulation monitors.

Fan diameter (mm)	**500**	**450**	**400**
Mean velocity across the monitored points (m/s)	19.3	12.7	12.1

As can be seen, there are significant reductions in air speed when changing fans, with no significant difference between 450 and 400 mm. In terms of heat, the behavior is as expected, with a 26% reduction in heat transfer capacity when reducing the size of the fan.

Without U cut-outs

The previous simulations indicate that the endshield wall, which interfaces with the frame and the deflector cover, significantly impacts airflow by obstructing its passage. The wall has U-shaped cuts that are filled with screw heads, allowing no air to pass through. Its negative effect is present in the tubes closest to this wall, as can be seen in the simulations presented so far, as they receive significantly less air than the others. The two solutions that were studied to diminish this negative effect are presented in Figure 19.

Figure 19 - Two options to remove U-cut-outs: (a) option 1, and (b) option 2.

(a) (b)

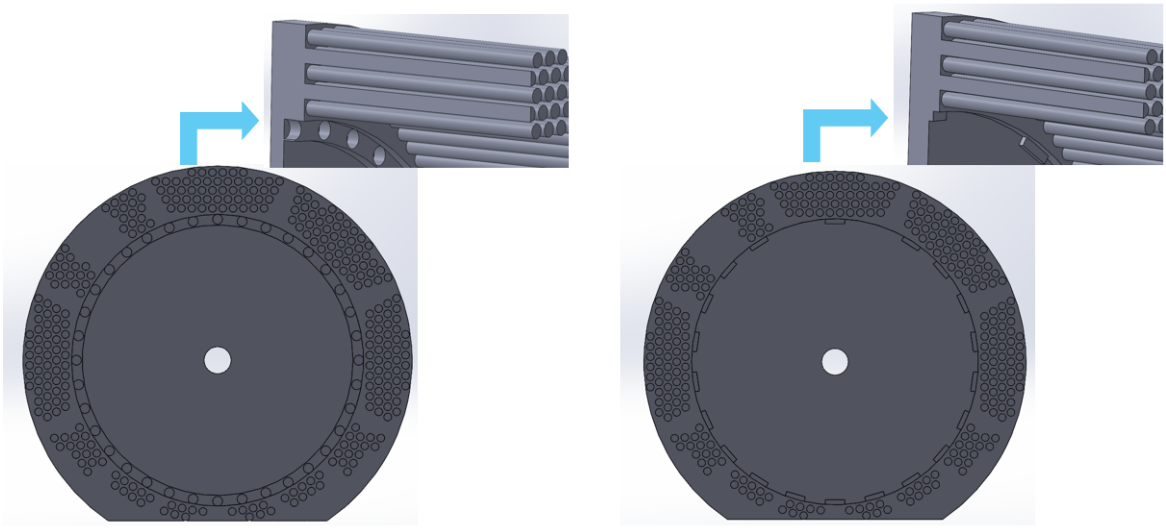

The solution on the left (option 1) consists of removing the U-shaped-cut-outs, allowing air to pass between the screw heads that enable the end shield to fit into the frame. The solution on the right (option 2) consists of reducing the thickness of the end shield from 45 to 25 mm and increasing the size of the air openings, without obstructing the screw. Both options aim to increase airflow and improve heat transfer from the tubes, which are closer to the heat source. Figure 20 shows how the air is distributed across the tubes in theses options and Table 12 shows the increase in air received by the tubes.

As it is possible to see, in general the amount of air received by the tubes is practically the same as before. On the other hand, in the case of the tubes located in the innermost radius, there is a 45% increase, in option one, and 53% increase, in option two, in the air speed reaching them. This is a very important effect, as it allows the tubes that are closer to the heat source to receive a lot more air. The effect of removing the U cut-outs is well visible in Figure 21.

Figure 20 - Air flow without U cut-outs for two options: (a) option 1, and (b) option 2.

(a) (b)

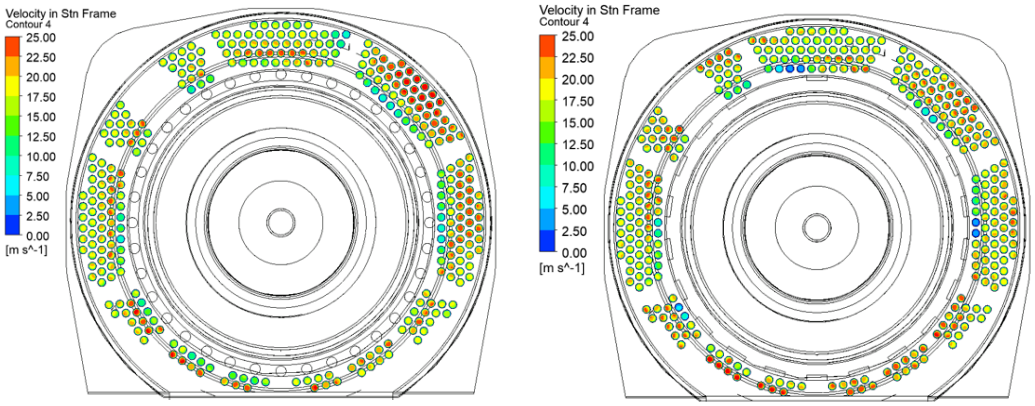

Table 12 - Mean air speed before and after this alteration.

Mean Total Velocity (m/s)	**Before**	**After**
Option 1	18.27	18.68
Option 2	18.27	18.73
Mean Interior Radius Velocity (m/s)		
Option 1	10.93	15.83
Option 2	10.93	16.70

Figure 21 - Comparison between the original and option 1 cases: (a) actual, and (b) option 1.

(a) (b)

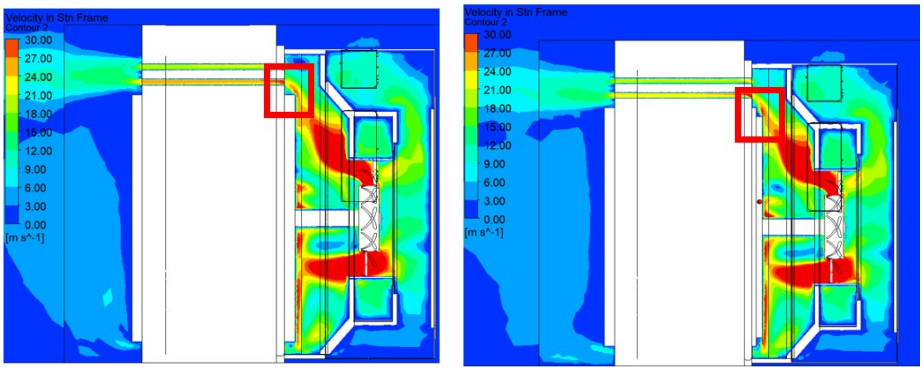

As highlighted in the red square, the removal of the U-shaped cut-out allowed for air to circulate more directly towards the tube and through the obstacle. This effect is similar to what was found on the literature, since the U-shaped cut-out in the end shield ends up functioning as a device that directs the air towards the tubes, just the study simulates (Liu & Ai, 2022). Their study concluded that air guidance aids have a significant impact on convection inside the tubes as also found here. In the Figure 22, the corresponding thermal behavior is shown.

It should be noted that there is a clear increase in overall heat transfer through all the tubes 5.4% and 5.8% and also a very considerable increase in the contribution of the innermost tubes 34% and 38%. There is no doubt that this simple design change can have a major effect on improving heat transfer. This conclusion results in significant monetary savings for the company, as the end shield becomes cheaper. Firstly, the part uses less material, making it lighter. Secondly, it requires fewer machining operations, in case of option 1, which speeds up the process.

Figure 22 - Heat absorbed for both options: (a) option 1, and (b) option 2.

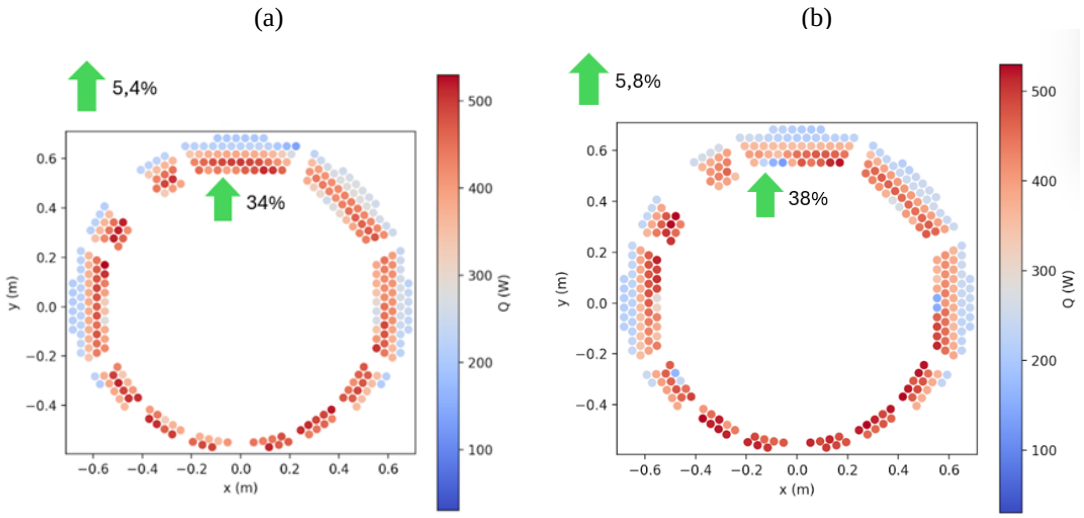

Without U cut-outs and less tubes

The previous solution has significantly enhanced the airflow and thermal performance of the inner tubes. In this research, the impact of tube removal on the volume of air reaching the remaining tubes and its subsequent influence on heat transfer efficiency were also studied. This investigation is based in the fact that exists an optimal tube number that maximizes heat transfer, as previously established in the literature (Yu & Meng, 2018).

The objective is to yield insights into the balance between the removal of tubes and the overall increase in air speed in the tube system and the reduction in heat transfer area. Since the thermal study is not based on actual real information, the removal of tubes was not based on their contribution to heat transfer, but only on their geometric position. Four options were tested for this study:

a) Test 1: Removal of external tube radius (r_6);

b) Test 2 - Removal of two external tube radius (r_5 and r_6);

c) Test 3 - Removal of internal tube radius (r_1 and r_2);

d) Test 4 - Removal of external and internal tube radius (r_1, r_2 and r_6).

Therefore, the removal of these pipes has the following implications for air flow; see Figure 23.

The removal of these tubes has significantly facilitated the flow of air to the remaining tubes. This enhancement is illustrated in the Table 13 below.

Table 13 - Tube removal effect on airflow and outlet temperature.

Sector	Tubes removed	Mean total velocity (m/s)	Increase (%)	$\dot{m}_{\text{total}}$ (kg/s)	T_{out} (°C)
Test 1	24	20.1	7.6	4.1	54.5
Test 2	84	24.0	32.4	4.0	49.0
Test 3	74	23.0	23.2	3.9	50.5
Test 4	98	22.1	18.5	3.4	51.5

These results clearly show that removing pipes significantly increase the air velocity passing through the pipe system, since with less tubes the air has fewer paths to follow. On the other hand, the total mass flow rate passing through the pipe system remains, practically, the same for the different tests. This is explained by the fact removing the tubes leads to higher pressure drop, as seen in Table 14, and then its curve system rises and intersects the fan curve higher up, in the head-flow rate curves already mentioned.

Figure 23 - Effect on airflow of removing the refereed tubes: (a) test 1, (b) test 2, (c) test 3, and (d) test 4.

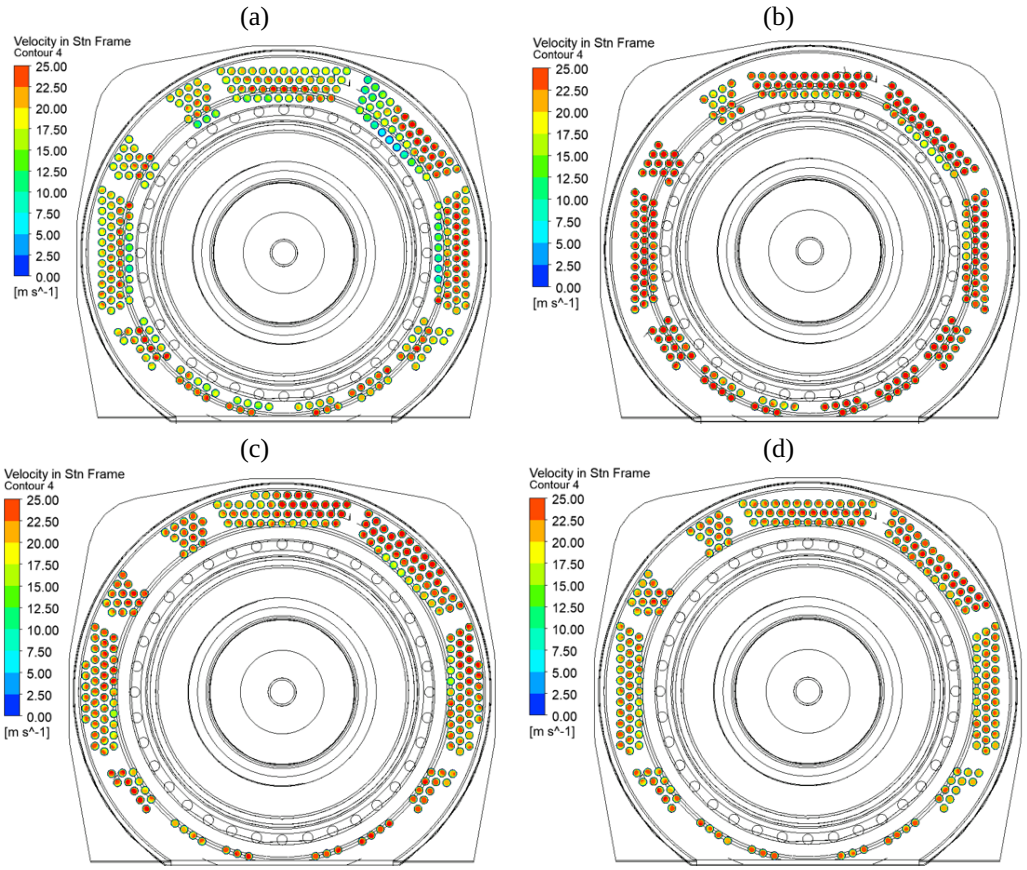

Table 14 - Tube removal effect on system pressure loss.

Situation	Pressure loss (Pa)
All tubes without front deflector	277
Less tubes (test 2) without front deflector	545

However, as this is an axial fan, their head-flow rate curves are almost vertical for long flow ranges and, as such, the new operating point is close across the different cases, leading to similar mass flow-rates across the tests. The corresponding thermal behavior is present in Figure 24, and the percentages represent the increase/decrease in heat removed to the situation with all tubes.

Thermal behavior reveals that removing the pipes, despite significantly increasing the air velocity passing through the system, does not improve heat transfer in tests 2, 3 and 4. A literature study justified the loss of heat removal capacity with the removal of tubes, in a heat exchanger, by the fact that the speed is higher in the system and the residence time in it is lower, causing the air to heat up less (Abeykoon, 2020).

However, in the present study, as can be seen in the Table 13, when comparing the air temperature at the outlet, it can be seen that in test 1, where considerably fewer tubes are removed, the air, in fact, heats up more, but only by a few degrees. Furthermore, from the analytical calculations, it has already been mentioned that only at very high speeds does the air stop heating up.

Thus, the reason for the loss of heat removal is due more to the loss of heat transfer area than to the residence time of the air in the tube. However, a balance can be found between the heat transfer area loss and the increase in air speed, especially when verifying that by removing only the last radius of tubes (r_1), the heat transfer capacity remains virtually unchanged, increase in 1.8%.

It is important to notice that these advancements correlate with notable decreases in component costs, motor weight, and production time, since 24 tubes were removed. Given the annual volume of motors manufactured by a company, such improvements can result in substantial annual savings.

Figure 24 - Effect on thermal performance of removing the tubes (heat absorbed): (a) test 1, (b) test 2, (c) test 3, and (d) test 4.

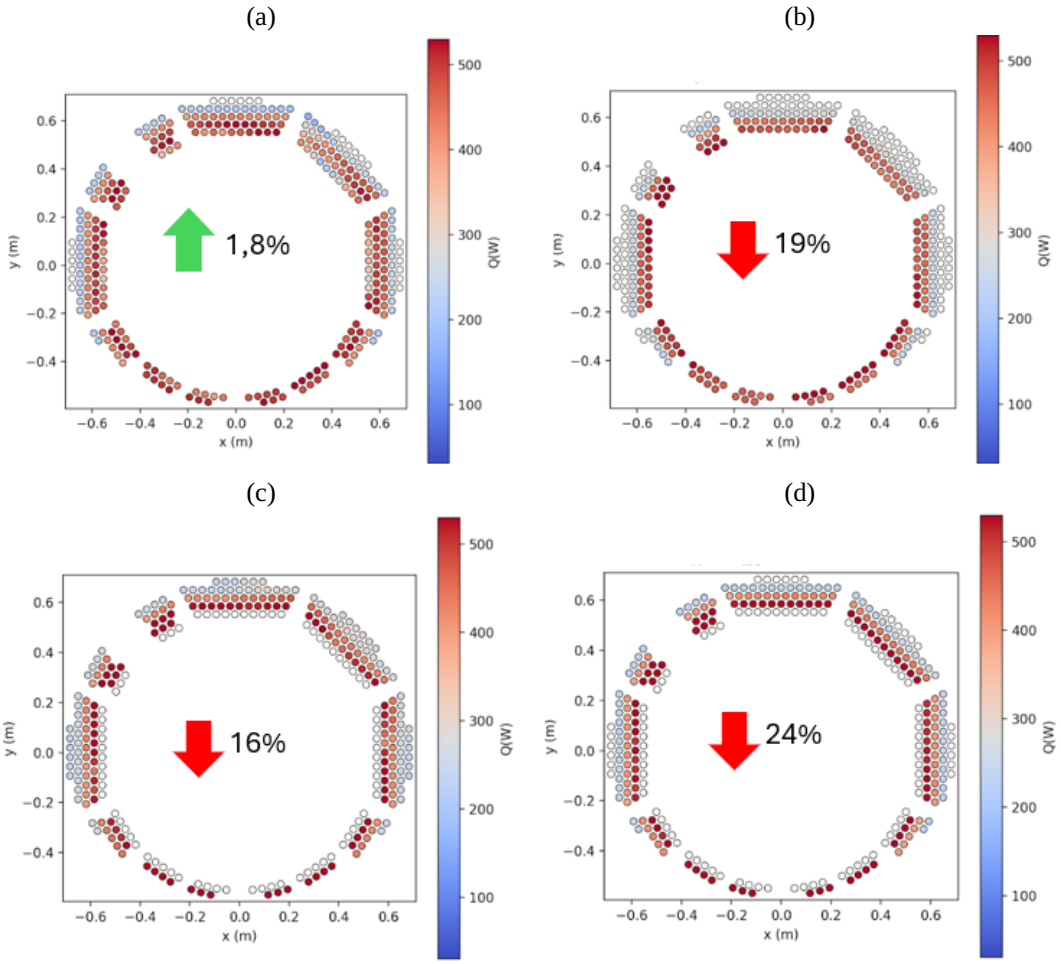

These peripheral tubes present an additional complicating factor: they obtain a reduced volume of internal air from the motor, resulting in a diminished convection effect surrounding the tube. The removal of these tubes could potentially influence, although not examined in this study, the reduction of pressure drop within the motor. This change would facilitate a more efficient and rapid circulation of internal air, which could ultimately benefit the overall performance of all the tubes involved, as also verified in the literature (Yu & Meng, 2018).

Note that the temperatures for the thermal load were adjusted to effectively compare the cases. Thus, the removal of outer tubes implied that the 60ºC temperature descends a radius or two. On the other hand, the removal of inner tubes, causes the radius of 105ºC to advance to the next one above.

As mentioned, removing tubes leads to an increase in pressure drop. The motor can also operate with the front deflector mounted in certain cases. Therefore, it is important to ensure that when removing a large number of tubes, as in test 2, the use of the front deflector does not introduce additional pressure drop such that it would fall outside the fan curve and prevent operation. Thus, the placement of the front deflector was simulated for test 2. Once again, its negative effect can be seen, but also that the fan was able to withstand the increase in pressure drop, indicating that in the tube removal scenario the use of the front deflector does not prevent operation.

Conclusions

This study successfully combined analytical and numerical approaches to better understand and optimize heat transfer in the pipe system of tube motors. We observed that the increasing air velocity within the pipe significantly enhances heat removal, with air velocity identified as the most influential factor in heat transfer. Also the pipe geometric attributes, such as length, thickness, and material are comparatively less critical for

heat transfer efficiency. Numerical analyses revealed the negative impact of the front deflector, 21% decrease in heat removal capacity, suggesting design optimization potential. Removing U cut-outs allowed more air to reach critical tubes, improving heat exchange (up to 6%). The removal of the outer 24 tubes maintained heat transfer capacity, which leads to substantial costs savings. Overall, this project not only deepened the understanding of heat transfer in tube motors but also produced practical solutions that can reduce material costs, lighten motor weight, and streamline production processes. In addition, it has enabled the development of a first iteration of a hybrid numerical-analytical tool that allows predicting the thermal behavior of tube motors for different changes that may be made. This way, whenever a designer wants to know if a change to the design, such as changing the position of the tubes, will greatly or slightly affect heat transfer in the motor, instead of conducting factory tests that take much longer and are impractical, they can use the model and have the answer the next day.

Acknowledgments

A. M. Afonso acknowledges FCT - Fundação para a Ciência e a Tecnologia for financial support through LA/P/0045 (ALiCE), UIDB/00532 and UIDP/00532 (CEFT), funded by national funds through FCT/MCTES (PIDDAC). For all their support throughout this project, thanks are due to Jorge Sousa, Hugo Campos and Daniel Pimenta.

Author Contributions

M. Costa: conceptualization, formal analysis, investigation, programs. **A. M. Afonso**: supervision, validation, visualization, writing – revision and editing.

Conflicts of Interest

The authors declare no conflict of interest.

References

Abeykoon, C. (2020). Compact heat exchangers – design and optimization with CFD. *International Journal of Heat and Mass Transfer*, *146*, 118766. https://doi.org/10.1016/j.ijheatmasstransfer.2019.118766

Ahmed, F., Roy, P., Towhidi, M., Feng, G., & Kar, N. C. (2019). CFD and LPTN Hybrid Technique to Determine Convection Coefficient in End-winding of TEFC Induction Motor with Copper Rotor. In Institute of Electrical and Electronics Engineers, *IECON 2019* [Proceedings]. 45th Annual Conference of the IEEE Industrial Electronics Society, Lisbon, Portugal. https://doi.org/10.1109/IECON.2019.8926651

ANSYS. (2021a). *Ansys CFX-Solver Modeling Guide*. Release 2021 R2. Ansys.

ANSYS. (2021b). *Ansys CFX-Solver Theory Guide* (Version 2021 R2). Ansys. https://dl.cfdexperts.net/cfd_resources/Ansys_Documentation/CFX/Ansys_CFX-Solver_Theory_Guide.pdf

Azeez, A. A., Olusegun, O., & Dare, S. (2024). Increase in performance efficiency of a heat exchanger through construction modification. *International Journal of Research Publication and Reviews*, *5*(5), 3271–3279. https://doi.org/10.55248/gengpi.5.0524.1221

Bergman, T. L., Lavine, A. S., Incropera, F. P., & DeWitt, D. P. (2011). *Fundamentals of Heat and Mass Transfer* (7th ed.). John Wiley & Sons.

de Paula Ferreira, A. (2013). *Sizing of heat exchangers air-to-air in three-phase induction electric motors* [Master's Thesis, Faculdade de Engenharia da Universidade do Porto].

Eletrobrás, Procel, Instituto Euvaldo Lodi, & Confederação Nacional da Indústria. (2009). *Motor elétrico: guia básico*. https://arquivos.portaldaindustria.com.br/app/conteudo_18/2014/04/22/6281/Motor_eletrico.pdf

Gronwald, P.-O., & Kern, T. A. (2021). Traction Motor Cooling Systems: A Literature Review and Comparative Study. *IEEE Transactions on Transportation Electrification*, *7*(4), 2892–2913. https://doi.org/10.1109/TTE.2021.3075844

International Electrotechnical Commission (IEC). (2020). *IEC 60034-6: Rotating Electrical Machines – Methods of Cooling (IC Code)*. https://www.iec.ch

International Energy Agency. (2021). *World Energy Outlook 2021*. IEA. https://www.iea.org/reports/world-energy-outlook-2021

Liu, J., & Ai, M. (2022). Structural optimization design and heat transfer characteristics of air-to-air cooled high voltage motor heat exchanger. *Case Studies in Thermal Engineering*, *40*, 102532. https://doi.org/https://doi.org/10.1016/j.csite.2022.102532

Louw, F. G., Backström, T. V., & Spuy, S. V. D. (2014). Investigation of the flow field in the vicinity of an axial flow fan during low flow rates. In American Society of Mechanical Engineers, *Conference Proceedings Turbo Expo* (Vol. 1A: Aircraft Engine; Fans and Blowers) [Proceedings]. ASME Turbo Expo 2014: Turbine Technical Conference and Exposition, Düsseldorf, Germany. https://doi.org/10.1115/GT2014-25927

Munson, B. R., Okiishi, T. H., Huebsch, W. W., & Rothmayer, A. P. (2012). *Fundamentals of Fluid Mechanics* (7th ed.). Wiley.

Nailen, R. L. (1975). Understanding the TEWAC Motor. *IEEE Transactions on Industry Applications*, *IA-11*(4), 350–355. https://doi.org/10.1109/TIA.1975.349307

Nasa Glenn Research Center. (2021). *Examining Spatial (Grid) Convergence*. https://www.grc.nasa.gov/www/wind/valid/tutorial/spatconv.html

Raman, R., Dewang, Y., & Raghuwanshi, J. (2018). A review on applications of computational fluid dynamics. *International Journal of LNCT*, *2*(6), 1–7. https://www.ijlnct.org/paper-directory/volume-2/issue-6/6.pdf

Soler & Palau Ventilation Group. (2025). *Catálogo de ventiladores axiais AVR (J)* [Código: AVR-042_2025-J]. https://solerpalau.com.br/biblioteca/produto/043/AVR-042_2025-J.pdf

Stockton, C. A., McElveen, R. F., & Chastain, E. (2024). The integral role of electric motors in achieving sustainability. *IEEE Transactions on Industry Applications*, *60*(5), 7949–7957. https://doi.org/10.1109/TIA.2024.3408721

Sung, S.-C., Kim, S.-K., & Oh, M.-D. (2021). Numerical analysis of the cooling performance of a totally enclosed air-to-air cooled motor using a dual cell heat exchanger model. *Journal of Mechanical Science and Technology*, *35*(6), 2719–2731. https://doi.org/10.1007/s12206-021-0542-z

Tan, C., Yap, W., Cheah, J., Yi Tien, E. W., Huey, J., Didane, D., Manshoor, B., & Elshayeb, S. (2024). CFD simulation and analysis of a fin and tube heat exchanger: Impact of air mass flow rate on thermal performance. *Journal of Designg for Sustainable and Environment*, *6*(2), 14–22. https://tinyurl.com/22ztgekx

Trivellato, F., & Raciti Castelli, M. (2015). Appraisal of Strouhal number in wind turbine engineering. *Renewable and Sustainable Energy Reviews*, *49*, 795–804. https://doi.org/10.1016/j.rser.2015.04.127

Wang, X., Li, B., Gerada, D., Huang, K., Stone, I., Worrall, S., & Yan, Y. (2022). A critical review on thermal management technologies for motors in electric cars. *Applied Thermal Engineering*, *201*, 117758. https://doi.org/https://doi.org/10.1016/j.applthermaleng.2021.117758

WEG S.A. (2024). *Guia de especificação de motores elétricos*. https://static.weg.net/medias/downloadcenter/h32/hc5/WEG-motores-eletricos-guia-de-especificacao-50032749-brochure-portuguese-web.pdf

White, F. M. (2006). *Viscous Fluid Flow* (3rd ed.). McGraw-Hill.

Wierda, L., & Zanutthi, A. (2024). *Ecodesign Impact Accounting Overview Report 2024*. https://www.vhk.nl/downloads/Reports/EIA/2024%20EIA%20IV%20Overview%20Report.pdf

Wilcox, D. C. (2006). *Turbulence Modeling for CFD* (3rd ed.). DCW Industries.

Yu, X., & Meng, D. (2018). Design analysis and improvement of cooler in positive-pressure explosion-proof low-speed high-capacity induction motors. *Applied Thermal Engineering*, *129*, 1002–1009. https://doi.org/https://doi.org/10.1016/j.applthermaleng.2017.10.101